Journal of Magnetic Resonance 208 (2011) 243–255

Contents lists available at ScienceDirect

Journal of Magnetic Resonance

journal homepage: www.elsevier.com/locate/jmr

A fast random walk algorithm for computing the pulsed-gradient spin-echo signal in multiscale porous media

Denis S. Grebenkov *

Laboratoire de Physique de la Matière Condensée, CNRS – Ecole Polytechnique, F-91128 Palaiseau, France

ARTICLE INFO

Article history:
Received 30 August 2010
Revised 3 November 2010
Available online 17 November 2010

Keywords:
Monte Carlo
Fast random walk
Restricted diffusion
Confinement
PGSE
NMR

ABSTRACT

A new method for computing the signal attenuation due to restricted diffusion in a linear magnetic field gradient is proposed. A fast random walk (FRW) algorithm for simulating random trajectories of diffusing spin-bearing particles is combined with gradient encoding. As random moves of a FRW are continuously adapted to local geometrical length scales, the method is efficient for simulating pulsed-gradient spin-echo experiments in hierarchical or multiscale porous media such as concrete, sandstones, sedimentary rocks and, potentially, brain or lungs.

1. Introduction

Many biological and industrial processes involve molecular diffusion in complex media: oxygen and nutrients transport in cells, tissues and organs [1–6], chemical reactions on catalytic surfaces [7–9], oil permeation in sedimentary rocks [10–12], setting of a concrete [13,14], etc. Being the intrinsic transport mechanism, restricted diffusion is an important source of information about the confining geometry [15,16]. So, diffusion-weighted nuclear magnetic resonance (NMR) imaging is a broadly applied non-invasive experimental technique for studying human organs (e.g., brain, lungs, kidneys) and natural or artificial materials (e.g., sandstones, sedimentary rocks, concrete) [17–22].

A standard pulsed-gradient spin-echo (PGSE) experiment starts with a 90° radio-frequency (rf) pulse that flips the nuclear magnetization into the transverse plane [17]. In a spatially inhomogeneous magnetic field $B(\mathbf{r})$, the nuclei precess with the Larmor frequency $\gamma B(\mathbf{r})$, γ being the nuclear gyromagnetic ratio (throughout the text, vectors are written in bold). Since the precession is faster or slower depending on the spatial position $\mathbf{r}$, the trajectory of a spin-bearing particle is "encoded" by the applied magnetic field as

$$\varphi = \int_0^t dt' \gamma B(\mathbf{r}(t')), \tag{1}$$

where φ is the random dephasing of the nucleus acquired along its Brownian trajectory $\mathbf{r}(t')$ up to an acquisition time t. The free induction decay (FID) is then obtained by averaging the nuclear transverse magnetization $e^{i\varphi}$ over all Brownian trajectories $\mathbf{r}(t')$ started uniformly in a given domain Ω:

$$\frac{E}{E_0} = \mathbb{E}\{e^{i\varphi}\}, \tag{2}$$

where E_0 is the reference signal (without applied magnetic field) which may account for bulk relaxation. The signal attenuation E/E_0 depends on physical parameters (applied magnetic field $B(\mathbf{r})$, acquisition time t, diffusion coefficient D, etc.) and the shape of the diffusion-confining domain Ω. The spin-echo and other echo sequences can be implemented by putting in Eq. (1) an effective temporal profile of the applied magnetic field (see [16,23,24] for details).

An explicit dependence of the signal on physical parameters (e.g., acquisition time t) can be derived only for unrestricted diffusion in the whole space. Among various numerical approaches which were employed to calculate the signal in confining domains, we focus on Monte Carlo techniques [25,26]. These techniques consist in simulating a representative set of Brownian trajectories $\mathbf{r}(t')$, calculating the acquired dephasing φ according to Eq. (1), and approximating the expectation in Eq. (2) by a large but finite sum of simulated outcomes. For relatively simple domains (e.g., slab, cylinder or sphere), basic Monte Carlo simulations with a fixed-time step δ can be used. Each Brownian trajectory $\mathbf{r}(t')$ is approximated by a sequence of t/δ independent normally distributed random jumps along each coordinate, with mean zero and variance $2D\delta$ [27–31]. Geometrical restrictions are implemented through the appropriate boundary condition. The integral in Eq. (1) is naturally approximated by a finite sum with the small time step δ:

* Fax: +33 169334799.
E-mail address: denis.grebenkov@polytechnique.edu

1090-7807/$ - see front matter © 2010 Elsevier Inc. All rights reserved.
doi:10.1016/j.jmr.2010.11.009

$$\varphi \approx \delta \sum_{k=1}^{t/\delta} \gamma B(\mathbf{r}(k\delta)). \tag{3}$$

Although these fixed-time step simulations are easy to implement, they are inefficient in hierarchical or *multiscale* porous media because the time step δ must be chosen very small in order to make the average one-step displacement $\sqrt{2D\delta}$ much smaller than the smallest geometrical feature of the domain, while most particles are released inside large pores. As a consequence, a very large number of steps (t/δ) may be required for simulating each trajectory. This is the major drawback of basic Monte Carlo schemes.

Leibig suggested to use fast random walks (FRWs), or so-called variable-time step simulations, to overcome this problem in the special case of surface relaxation (without gradients) [32]. In FRWs, the length and time of each random jump of a particle are adapted to the local geometrical structure surrounding the particle, in order to explore the confining domain as fast as possible (Fig. 1). Inside small pores, the particle moves by tiny jumps, which become much larger when the particle enters large pores. Making the time step δ adaptable, one removes the major drawback of basic Monte Carlo techniques. On the contrary, the computation of the dephasing φ in Eq. (1) for gradient encoding, which was elementary for basic Monte Carlo simulations with a fixed-time step, now becomes a challenging problem. In fact, an approximate integration in Eq. (3) fails for variable (and potentially large) time steps.

In this paper, we provide a mathematical solution to this problem which allows one to profit the computational advantages of FRWs in simulating PGSE signals. This novel variable-time step technique can be implemented to calculate the signal attenuation in a wide range of model and realistic porous media, in which the largest and smallest pore sizes differ by orders of magnitude. Examples range from random packs of spheres or self-similar fractals, to multiscale porous media such as concrete, sandstones, sedimentary rocks and, potentially, brain or lungs.

The paper is organized as follows. In the next section, we describe the fast random walk algorithm and explain the implementation of the gradient encoding. Section 3 is devoted to comments, numerical checks, further extensions and improvements. Appendices describe the mathematical ground for the derivation of the main results of the paper. Since the analytical results are provided self-consistently in the main text, practical "users" of the algorithm may skip the technical details in Appendices. However, the presented mathematical derivation is essential for understanding the employed approximations and for further extensions of the algorithm, e.g., to semi-permeable structures.

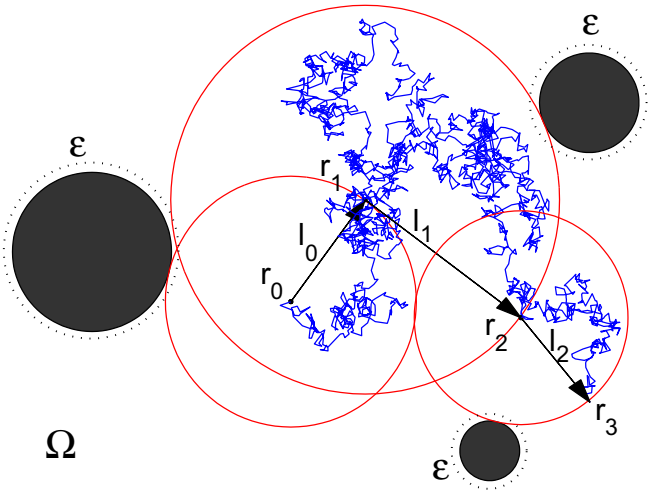

Fig. 1. A fast random walk in a medium Ω with obstacles (dark disks). From an initial position $\mathbf{r}_0$, one determines the distance ℓ_0 to the obstacles (or to the boundary of the domain) and draws a circle of radius ℓ_0 centered at $\mathbf{r}_0$. A "jump" to a randomly (uniformly) chosen point on the circle is then executed. This single large displacement (shown by an arrow) replaces a detailed simulation of Brownian trajectory inside the disk of radius ℓ_0. From the new point $\mathbf{r}_1$, one determines the distance again and executes the next jump, and so on (only three jumps are shown).

2. Fast random walk algorithm

The concept of fast random walks was proposed by Muller [33] in 1956 and then broadly employed by many authors, for instance, to study diffusion–reaction processes and related first-passage problems in random packs of spheres [34,35] or near prefractal boundaries [36–38]. The idea consists in replacing Brownian motion by an equivalent "spherical process" that explores the confining domain as fast as possible. To illustrate the idea, we consider a particle which starts to diffuse from an initial position $\mathbf{r}_0$ (Fig. 1). Let us draw the largest disk (or ball in three dimensions) which is centered at $\mathbf{r}_0$ and inscribed in the confining medium. Its radius ℓ_0 is the distance between $\mathbf{r}_0$ and the boundary. After wandering inside the disk during a random time τ_1, the particle exits the disk at random point $\mathbf{r}_1$. Since there was no "obstacles" inside the disk, all the exit points of the disk are equally accessible for isotropic Brownian motion so that the exit point $\mathbf{r}_1$ has a uniform distribution on the circle of radius ℓ_0. From $\mathbf{r}_1$, the new largest disk of radius ℓ_1 is inscribed in the confining domain. After wandering inside the disk during a random time τ_2, the particle exits at random point $\mathbf{r}_2$, and so on. Following the Brownian trajectory of the particle, one can construct the sequence of inscribed disks (i.e., their centers $\mathbf{r}_n$ and radii ℓ_n) and the associated exit times τ_n.

The fundamental idea behind FRWs is that the sequence $\{\mathbf{r}_n, \ell_n, \tau_n\}$ can be constructed directly, without simulating the underlying Brownian trajectory at all. At each step, one determines the distance ℓ_n between the current position $\mathbf{r}_n$ and the boundary of the confining domain and chooses the next position $\mathbf{r}_{n+1}$ randomly and uniformly on the circle of radius ℓ_n. The time τ_{n+1} needed to exit from the disk (i.e., to jump from $\mathbf{r}_n$ to $\mathbf{r}_{n+1}$) is a random variable which can be easily generated from the well-known probability distribution (Section 2.1). A detailed time-consuming simulation of a Brownian trajectory with high spatial resolution is therefore replaced by generation of random jumps which are adapted to the local geometrical structure of the domain. In other words, the spatial resolution of the new simulated process is constantly adapted to the distance to the boundary: closer the particle to the boundary, finer the simulation scale. Performing each jump at largest possible distance yields a tremendous gain in computational time.

2.1. Generation of exit times

The time τ needed for Brownian motion to exit from a domain is a random variable. Its probability distribution, $S_0(t) \equiv \mathbb{P}\{\tau > t\}$, which is also known as the survival probability (i.e., the probability for a particle to survive or to remain inside the domain up to time t), admits a spectral representation [cf. Eq. (B.1)]. For the unit disk and the unit sphere with absorbing (Dirichlet) boundary condition, the Laplacian eigenfunctions and eigenvalues are given in Appendix by Eqs. (A.15) and (A.19), from which one retrieves the classical formulas for the survival probability for Brownian motion started from the origin:

$$S_0(t) = 2\sum_{k=0}^{\infty} \frac{1}{\alpha_{0k} J_1(\alpha_{0k})} e^{-\alpha_{0k}^2 t} \quad (d=2), \tag{4}$$

$$S_0(t) = 2\sum_{k=0}^{\infty} (-1)^k e^{-\alpha_{0k}^2 t} \quad (d=3), \tag{5}$$

with the dimensionless time t, and $\{\alpha_{nk}\}$ is the set of all positive zeros (indexed by $k = 0,1,2,\ldots$) of

- Bessel function $J_n(z)$ of the first kind ($d = 2$), or
- spherical Bessel functions $j_n(z)$ of the first kind ($d = 3$).

The survival probability monotonously decreases from 1 at $t = 0$ to 0 as t goes to infinity (Fig. 2a). In the short-time limit, the exit probability $1 - S_0(t)$ is extremely small,

$$1 - S_0(t) \simeq \begin{cases} 2e^{-1/(4t)}(1 - t + 4t^2 + O(t^3)) & (d = 2), \\ 2e^{-1/(4t)}\frac{1}{\sqrt{\pi t}} & (d = 3), \end{cases} \quad (6)$$

because very few particles can cross the distance from the origin to the boundary during a short time. In turn, for large t, the survival probability decays exponentially,

$$S_0(t) \simeq \begin{cases} \frac{2}{\alpha_{00}J_1(\alpha_{00})}e^{-\alpha_{00}^2 t} & (d = 2), \\ 2e^{-\alpha_{00}^2 t} & (d = 3), \end{cases} \quad (7)$$

since it is unlikely for diffusing particles to avoid the encounter with the boundary during a long time.

Fig. 2b shows the probability density, $-\frac{dS_0(t)}{dt}$, of the exit time. This figure and the above asymptotic behaviors clearly indicate that the (normalized) exit time is localized around its mean value which is equal to $1/(2d)$. In particular, the probability that τ does not belong to an interval $(t_{\min}, t_{\max})$, can be made negligible by choosing $t_{\min}$ and $t_{\max}$ appropriately. For instance, if $t_{\min} = 0.001$ and $t_{\max} = 10$, one has

$$\mathbb{P}\{\tau \notin (0.001, 10)\} = 1 - S_0(0.001) + S_0(10) < 10^{-12d} \quad (d = 2, 3). \quad (8)$$

As a consequence, the exit times beyond this interval can be completely ignored.

The explicit form of Eqs. (4) and (5) allows one to generate exit times in a standard way. Inverting numerically the function $S_0(t)$ (i.e., finding a function $T_0(x)$ such that $S_0(T_0(x)) = x$ for any x between 0 and 1), one obtains a mapping from random variables χ_n with a uniform distribution on the unit interval, to the exit times

$$\tau_n = \frac{\ell_n^2}{D} T_0(\chi_n) \quad (9)$$

for the disk or sphere of radius ℓ_n and for a given diffusion coefficient D. The uniform random variables χ_n are generated by a routine function for pseudo-random numbers.

In summary, two preliminary numerical procedures are required for generating the exit times:

(1) Finding a finite number of positive zeros $\{\alpha_{0k}\}$ of Bessel function $J_0(z)$. The inequalities $\pi k < \alpha_{0k} < \pi(k + 1)$ allow one to search for a single zero on each interval $(\pi k, \pi k + \pi)$ by bisection method or Newton's method. Since smaller times require larger truncation sizes, the asymptotic formula (6) can be used instead of the truncated series in Eqs. (4) and (5) to improve the accuracy at short times. In three dimensions, this step is skipped because the positive zeros of the spherical Bessel function $j_0(z) = \sin(z)/z$ are: $\alpha_{0k} = \pi(k + 1)$.
(2) Constructing the function $T_0(x)$ as a numerical solution $T_0(x) = t$ of the equation $S_0(t) = x$ for a fine uniform mesh of points x. The monotonous decrease of $S_0(t)$ ensures, for any x, the unique solution which can be computed by bisection method or Newton's method.

Both procedures rely on classical numerical methods. Moreover, these procedures have to be performed once and forever while the stored values of the function $T_0(x)$ can be loaded before starting Monte Carlo simulations. As a consequence, the generation of the exit times during simulations is reduced, through Eq. (9), to a routine generation of uniformly distributed pseudo-random numbers.

2.2. Gradient encoding

In contrast to basic Monte Carlo simulations, the jump length in FRWs is set by the geometric constraints (distance to the boundary), while the time step is random. As time steps can now be large, the computation of the dephasing φ in Eq. (1) is a challenging problem.

From now on, we focus on a linear magnetic field gradient $\mathbf{g} = g_1\mathbf{e}_1 + \cdots + g_d\mathbf{e}_d$, where $\mathbf{e}_i$ are the unit vectors along each coordinate axis ($i = 1,\ldots,d$), and g_i are the projections of $\mathbf{g}$ onto these axes. The magnetic field inhomogeneity $B(\mathbf{r}) = (\mathbf{r}\cdot\mathbf{g})$ is the scalar product between $\mathbf{r}$ and $\mathbf{g}$ or, equivalently, the projection of the vector $\mathbf{r}$ onto the gradient $\mathbf{g}$. The total dephasing φ is

$$\varphi = \gamma(g_1\phi_1 + \cdots + g_d\phi_d),$$

where ϕ_i is the (random) normalized phase along the ith coordinate axis:

$$\phi_i = \int_0^t dt'(\mathbf{e}_i \cdot \mathbf{r}(t')). \quad (10)$$

Our goal is now to withdraw the trajectory $\mathbf{r}(t')$ by expressing the random variable ϕ_i in terms of the sequence $\{\mathbf{r}_n, \ell_n, \tau_n\}$ generated by a FRW algorithm.

For any random trajectory $\mathbf{r}(t')$, the sequence of inscribed disks (with their centers $\mathbf{r}_n$ and radii ℓ_n) and the associated exit times τ_n can be constructed, as described earlier. These disks (or balls in three dimensions) split the trajectory into successive parts, the

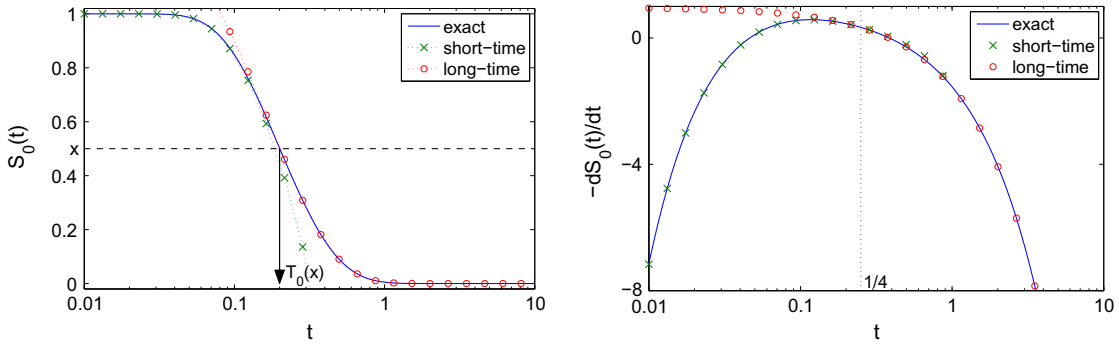

Fig. 2. Left: The survival probability $S_0(t)$ and its short-time and long-time asymptotic behaviors (6) and (7) for the unit disk (the curve for the unit sphere is similar and not shown). The dashed horizontal line at $S_0(t) = x$ illustrates the construction of the inverse function $T_0(x)$. Right: The probability density $-dS_0(t)/dt$ of the exit time and its short-time and long-time asymptotic behaviors derived from Eqs. (6) and (7). The vertical dotted line shows the mean exit time 1/4.

nth part having started at the center $\mathbf{r}_n$ of the nth disk at time $t_n = \sum_{j=1}^{n} \tau_j$ and exited this disk at $\mathbf{r}_{n+1}$ at time $t_{n+1} = t_n + \tau_{n+1}$. The number of these parts is also random. Since Brownian motion is a Markov process (no memory), each part of the trajectory, once its starting and arrival points are fixed, is independent from the other parts. As a consequence, the random dephasing $\delta\phi_{i,n}$ acquired along the ith coordinate axis during diffusion inside the nth disk,

$$\delta\phi_{i,n} = \int_{t_n}^{t_{n+1}} dt' (\mathbf{e}_i \cdot \mathbf{r}(t')) \quad (\mathbf{r}(t_n) = \mathbf{r}_n, \mathbf{r}(t_{n+1}) = \mathbf{r}_{n+1}, t_{n+1} = t_n + \tau_{n+1}), \tag{11}$$

is independent from the other parts of the trajectory. Figuratively speaking, the trajectory is "pinned" at points $\mathbf{r}(t_n) = \mathbf{r}_n$ ($n = 0, 1, 2, \ldots$) in order to determine the successive dephasing $\delta\phi_{i,n}$ separately from each other. Shifting the starting position and the starting time of the nth part of Brownian trajectory $\mathbf{r}(t')$ (between the "pinning" points $\mathbf{r}_n$ and $\mathbf{r}_{n+1}$), one can write $\mathbf{r}(t') = \mathbf{r}_n + \mathbf{w}_{t'-t_n}$, where $\mathbf{w}_{t'}$ is the Brownian motion started from the origin at time 0 ($\mathbf{w}_0 = 0$) and conditioned to exit the disk (ball) of radius $\ell_n = |\mathbf{r}_{n+1} - \mathbf{r}_n|$ at point $\mathbf{r}_{n+1} - \mathbf{r}_n$ at time τ_{n+1}: $\mathbf{w}_{\tau_{n+1}} = \mathbf{r}_{n+1} - \mathbf{r}_n$. In other words, the process $\mathbf{w}_{t'}$ represents the motion of a particle inside the nth disk, i.e., during one jump between $\mathbf{r}_n$ and $\mathbf{r}_{n+1}$. The acquired dephasing is then

$$\delta\phi_{i,n} = \int_{t_n}^{t_{n+1}} dt' (\mathbf{e}_i \cdot (\mathbf{r}_n + \mathbf{w}_{t'-t_n})) = \tau_{n+1} x_{i,n} + \int_0^{\tau_{n+1}} dt' (\mathbf{e}_i \cdot \mathbf{w}_{t'}),$$

where $x_{i,n} = (\mathbf{e}_i \cdot \mathbf{r}_n)$. The second term is a random variable which depends on three variables, τ_{n+1}, ℓ_n and $\mathbf{r}_{n+1} - \mathbf{r}_n$, which will be generated by a FRW algorithm, as well as on the trajectory $\mathbf{w}_{t'}$ inside the disk whose generation we want to avoid. If the conditional probability distribution of the second term (with fixed τ_{n+1}, ℓ_n and $\mathbf{r}_{n+1} - \mathbf{r}_n$) was known, one could generate this random variable at each step. Unfortunately, there is no easily computable formula for this distribution. We propose therefore to approximate this random variable by its mean value, averaged over all possible realizations of the process $\mathbf{w}_{t'}$. One of the main results of the paper is the explicit formula for this mean value which is derived in Appendix A. The dephasing $\delta\phi_{i,n}$ becomes

$$\delta\phi_{i,n} \simeq \tau_{n+1} x_{i,n} + \frac{\ell_n^2}{D} (x_{i,n+1} - x_{i,n}) \Phi_d\left(\frac{D\tau_{n+1}}{\ell_n^2}\right), \tag{12}$$

where ℓ_n^2/D is the rescaling factor, $(x_{i,n+1} - x_{i,n})/\ell_n$ represents $\cos\theta$ from Eq. (A.2), and

$$\Phi_2(t) = \frac{\sum_{k=0}^{\infty} \left[\frac{1}{\alpha_{0k} J_1(\alpha_{0k})} e^{-\alpha_{0k}^2 t} + \frac{1}{2J_0(\alpha_{1k})} e^{-\alpha_{1k}^2 t}\right]}{2\sum_{k=0}^{\infty} \frac{\alpha_{0k}}{J_1(\alpha_{0k})} e^{-\alpha_{0k}^2 t}}, \tag{13}$$

$$\Phi_3(t) = \frac{\sum_{k=0}^{\infty} \left[3(-1)^k e^{-\alpha_{0k}^2 t} - (-1)^k \sqrt{\alpha_{1k}^2 + 1}\, e^{-\alpha_{1k}^2 t}\right]}{4\sum_{k=0}^{\infty} (-1)^k \alpha_{0k}^2 e^{-\alpha_{0k}^2 t}}. \tag{14}$$

As earlier for $S_0(t)$ and $T_0(x)$, the function $\Phi_d(t)$ has to be computed once and forever on a fine mesh of times t between 0.001 and 10 (or even a shorter interval). In fact, the argument of the function $\Phi_d(t)$ in Eq. (12) is the normalized exit time, for which the inequality (8) excludes the values smaller 0.001 or larger 10. The short-time asymptotic behavior

$$\Phi_d(t) \simeq \frac{1}{2} t(1 - 2t) + O(t^3) \tag{15}$$

is useful for computing $\Phi_d(t)$ at $t < 0.1$ (see Appendix A). The accuracy of this approximation is illustrated by Fig. A.1.

One simulation run is continued until the time counter t_{n+1} exceeds the acquisition time t.

2.3. The last step

The last step is different from the others because the gradient encoding is switched off at the fixed acquisition time t, while the particle continues to diffuse inside the disk up to a later exit time t_{n+1} (without dephasing between t and t_{n+1}). In other words, the upper limit t_{n+1} of the integral in Eq. (11) has to be replaced by t for the last step:

$$\delta\hat{\phi}_i = \int_{t_n}^{t} dt' (\mathbf{e}_i \cdot \mathbf{r}(t')) \quad (\mathbf{r}(t_n) = \mathbf{r}_n, \mathbf{r}(t_{n+1}) = \mathbf{r}_{n+1}, t_{n+1} = t_n + \tau_{n+1}).$$

A rigorous consideration would consist in generating a random position of Brownian motion at the acquisition time t inside the disk and computing the corresponding phase shift. Although it is feasible in theory, a practical implementation would significantly slow down simulations. We propose two approximate solutions to this problem.

The first solution is a natural extension of the previous analysis when the contribution $\Phi_d(t)$ in Eq. (12) would be replaced by another one with the upper limit t instead of t_{n+1}. This new contribution, which depends on both time variables t and t_{n+1}, is mentioned in Appendix A. Although the explicit form (A.14) allows for an accurate preliminary computation, the dependence on two variables requires a lot of stored data. For this reason, we do not employ Eq. (A.14) and propose below the second approximate solution.

Since the final position of the particle at the acquisition time t is irrelevant, one can average over all the final positions. The averaged first moment of the acquired dephasing is strictly zero because of the rotational symmetry. In turn, the second moment is a measure of fluctuations of the random dephasing during the last step. At first thought, one could suggest to take the second moment of the dephasing due to unrestricted diffusion which is equal to $2D(t - t_n)^3/3$. However, this naive approximation ignores the fact that the particle is conditioned to remain inside the disk of radius ℓ_n up to the acquisition time t (since the exit time t_{n+1} exceeds t). In Appendix B, we take this condition into account and calculate the conditional second moment of the dephasing. The last increment of the phase can then be approximated as

$$\delta\hat{\phi}_i = (t - t_n) x_{i,n} + \sqrt{2D(t - t_n)^3/3}\, \widehat{\Phi}_d\left(\frac{(t - t_n)D}{\ell_n^2}\right)\eta, \tag{16}$$

where η is a Gaussian random variable with mean zero and variance 1. The function $\widehat{\Phi}_d(t)$ that accounts for the restricted character of diffusion, is defined in such a way that $(2t^3/3)[\widehat{\Phi}_d(t)]^2 = S_2(t)/S_0(t)$ is the conditional second moment of the dephasing up to time t inside the unit disk (or ball) with absorbing boundary condition, i.e.,

$$\widehat{\Phi}_d(t) = \sqrt{\frac{S_2(t)/S_0(t)}{2t^3/3}}, \tag{17}$$

where $S_2(t)$ is the second moment for survived particles and $S_0(t)$ is the survival probability from Section 2.1. In Appendix B, we derived the exact explicit formulas for $S_2(t)$ for the unit disk ($d = 2$),

$$S_2(t) = -\frac{1}{48}\sum_{k=0}^{\infty} \frac{\alpha_{0k}}{J_1(\alpha_{0k})} (3\alpha_{0k}^{-4} - 56\alpha_{0k}^{-6} + 288\alpha_{0k}^{-8}) e^{-\alpha_{0k}^2 t} - \frac{1}{2}\sum_{k=0}^{\infty} \frac{1}{\alpha_{1k}^4 J_0(\alpha_{1k})} e^{-\alpha_{1k}^2 t} + \frac{t}{6}\sum_{k=0}^{\infty} \frac{\alpha_{0k}}{J_1(\alpha_{0k})} (\alpha_{0k}^{-4} + 4\alpha_{0k}^{-6}) e^{-\alpha_{0k}^2 t}, \tag{18}$$

and for the unit sphere ($d = 3$)

$$S_2(t) = \frac{1}{24}\sum_{k=0}^{\infty}(-1)^k\left(-\alpha_{0k}^{-2} + 17\alpha_{0k}^{-4} - 174\alpha_{0k}^{-6}\right)e^{-\alpha_{0k}^2 t} + \frac{5}{12}\sum_{k=0}^{\infty}\frac{(-1)^k\sqrt{\alpha_{1k}^2+1}}{\alpha_{1k}^4}e^{-\alpha_{1k}^2 t} + \frac{t}{12}\sum_{k=0}^{\infty}(-1)^k\left(4\alpha_{0k}^{-2} + 3\alpha_{0k}^{-4}\right)e^{-\alpha_{0k}^2 t}. \quad (19)$$

The coefficients in these formulas are fully expressed in terms of zeros α_{0k} and α_{1k}. In practice, the above infinite series are truncated (the required accuracy being controlled by the truncation size) and the function $\widehat{\Phi}_d(t)$ is evaluated numerically for on a fine mesh of times t between 0.001 and 10. As earlier, the function $\widehat{\Phi}_d(t)$ has to be computed once and forever, *before* starting Monte Carlo simulations. When the simulations are running, the stored values of $\widehat{\Phi}_d(t)$ are plugged into Eq. (16), eventually with an appropriate interpolation. In other words, even if the explicit formulas for $\widehat{\Phi}_d(t)$ may look complicated, this step does not slow down Monte Carlo simulations.

2.4. Boundary condition

The presence of a boundary is the major complication for restricted diffusion. Various physical processes may happen with a nucleus near or at the boundary (e.g., relaxation or permeation). Since the jump length is equal to the distance to the boundary, a particle may approach the boundary infinitely close but never hits it. One has therefore to consider a surface layer of a finite thickness ε. When the distance to the boundary is smaller than ε, the particle "interacts" with the boundary. One of the three boundary conditions is usually implemented in order to account for this interaction:

(1) Dirichlet boundary condition mimics the situation when the nucleus either completely loses its magnetization, or leaves the domain through a (perfectly) permeable wall and never returns; in both cases, the nucleus does not contribute to the FID, and the simulation of its trajectory is terminated;
(2) Neumann boundary condition states that the magnetization is not affected at all, the nucleus is just moved away from such a reflecting boundary, and the simulation is resumed;
(3) Robin boundary condition realizes a random choice between the above outcomes with a given reflection probability (which in turn is determined by surface relaxivity or membrane permeability).

The Dirichlet boundary condition has the simplest implementation: the simulation is terminated whenever the nucleus approached the boundary closer than ε. However, boundaries are almost reflecting in many NMR applications, and we focus here on Neumann boundary condition. An extension of the algorithm to Robin boundary condition, which seems to be possible, is beyond the scope of the paper.

When a particle reaches the boundary, it should be somehow "released" in an interior point of the confining domain to continue diffusive motion. The most usual way for implementing reflection is to move the particle to a fixed distance from the boundary. This distance is close to the surface layer thickness ε, and the particle continues diffusive motion by small jumps (in the order of ε). As a consequence, a lot of computational time is wasted for a too detailed simulation of Brownian trajectory near the boundary. In what follows, we propose a more efficient solution.

If $\mathbf{r}_n$ is the current position of the particle near the boundary $\partial\Omega$ (i.e., $|\mathbf{r}_n - \partial\Omega| < \varepsilon$), one finds the boundary point $\mathbf{r}'_n \in \partial\Omega$ which is the closest to $\mathbf{r}_n$, and take a disk (or ball) centered at $\mathbf{r}'_n$ and of some radius R such that $\varepsilon \ll R \ll a$, where a is the characteristic length scale of the boundary near $\mathbf{r}_n$ (e.g., its radius of curvature). On the one hand, the disk should be as large as possible for performing a bigger jump and thus reducing computational time. On the other hand, the disk should be small enough so that the part of the boundary delimited by this disk can be treated as flat (Fig. 3). Since the boundary is reflecting, one can consider Brownian trajectory in the whole disk (even outside the confining domain) and then reflect the exterior part of the trajectory in respect to the (locally flat) boundary. In particular, if the first encounter with the disk occurs outside the confining domain (as illustrated on Fig. 3), the hitting point A should be reflected to its mirror point $\mathbf{r}_{n+1}$. For the reflected Brownian motion inside the disk (or ball), the mean phase shift during the jump from $\mathbf{r}_n$ to $\mathbf{r}_{n+1}$ is computed in Appendix C that yields the increment for the reflection step:

$$\delta\tilde{\phi}_{i,n} = \tau_{n+1}x_{i,n} + \mathbf{n}_i\frac{R^3}{D}\widetilde{\Phi}_d\left(\frac{D\tau_{n+1}}{R^2}\right) + \frac{x_{i,n+1} - \mathbf{n}_i(\mathbf{r}_{n+1}\cdot\mathbf{n})}{|\mathbf{r}_{n+1} - \mathbf{n}(\mathbf{r}_{n+1}\cdot\mathbf{n})|} \times \frac{R^3}{D}\Phi_d\left(\frac{D\tau_{n+1}}{R^2}\right), \quad (20)$$

where $\mathbf{n}$ is the unit normal vector at the boundary point $\mathbf{r}'_n$ pointing towards the interior of the confining domain, $\mathbf{n}_i = (\mathbf{n}\cdot\mathbf{e}_i)$, $\Phi_d(t)$ was earlier defined by Eqs. (13) and (14), and the new function $\widetilde{\Phi}_d(t)$ is

$$\widetilde{\Phi}_2(t) = \frac{t}{4} + \frac{\sum_{k=0}^{\infty}\left(i_k^{(1)} - t i_k^{(2)}\right)e^{-\alpha_{0k}^2 t}}{\sum_{k=0}^{\infty}\frac{\alpha_{0k}}{J_1(\alpha_{0k})}e^{-\alpha_{0k}^2 t}}, \quad (21)$$

$$\widetilde{\Phi}_3(t) = \frac{t}{4}, \quad (22)$$

with the coefficients $i_k^{(1)}$ and $i_k^{(2)}$ given by Eq. (C.1) (see discussion in Appendix C). Quite surprisingly, the function $\widetilde{\Phi}_3(t)$ has a much simpler form than its two-dimensional counterpart $\widetilde{\Phi}_2(t)$. Once again, the function $\widetilde{\Phi}_2(t)$ has to be computed once and forever. We propose a simple empirical approximation

$$\widetilde{\Phi}_2(t) \simeq \begin{cases} \frac{1}{4}t(1 - 0.75t) & t < 0.12, \\ 0.212t + 0.00283 & t > 0.12. \end{cases}$$

The maximum relative error of this approximation is 1.7% (at $t = 0.12$). It is worth stressing that this relation is based on the numerical computation of the $\widetilde{\Phi}_2(t)$, in contrast to other approximate relations in the paper which were rigorously derived by analytical methods.

Since the surface layer thickness ε is chosen to be very small, the distinction between $\mathbf{r}_n$ and $\mathbf{r}'_n$ can be ignored. The advantage of the reflection step is that a particle is moved relatively far away from the boundary so that further jumps will be much larger than ε.

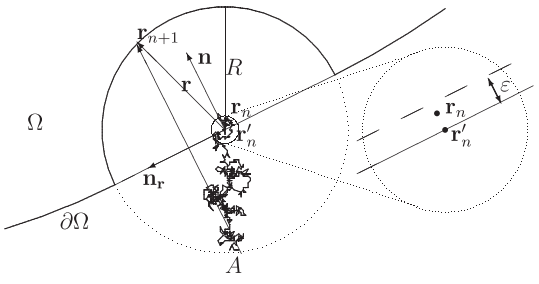

Fig. 3. When the particle has approached the reflecting boundary $\partial\Omega$ closer than ε, it is "released" on a circle of radius R centered at the encounter boundary point $\mathbf{r}'_n$. If the released point A does not belong to the confining domain Ω, one uses its mirror reflected point $\mathbf{r}_{n+1}$ inside Ω. The radius R should be chosen as large as possible, but small enough in comparison to the characteristic length of the boundary (so that the boundary is almost flat at scale R).

2.5. Algorithm

One simulation run starts from a randomly chosen initial point $\mathbf{r}_0$ and generates iteratively the successive positions $\mathbf{r}_n$ at times t_n and the acquired phase increments $\delta\phi_{i,n}$ (or $\delta\tilde{\phi}_{i,n}$, or $\delta\hat{\phi}_i$) along each coordinate axis (Fig. 4). The simulation run is terminated when the time counter exceeds the acquisition time t. The output of one simulation run is a set of accumulated phases ϕ_i along each coordinate axis ($i = 1\ldots d$). Launching the algorithm N times, one obtains N random realizations $\{\phi_i^j\}(j = 1\ldots N)$ of these phases, i.e., their empirical distributions. After that, the signal attenuation as a function of the gradient $\mathbf{g}$ is approximated as

$$\frac{E(\mathbf{g})}{E_0} \simeq \frac{1}{N}\sum_{j=1}^{N} \exp\left[i\gamma \sum_{i=1}^{d} g_i \phi_i^j\right] \tag{23}$$

(the imaginary unit i in front of γ should not be confused with the summation index i). Since the signal attenuation is computed *after* obtaining the empirical distributions of ϕ_i, there is no need to restart Monte Carlo simulations for each gradient direction and intensity. This is a significant advantage of Monte Carlo techniques in comparison to finite difference or finite element methods which solve the Bloch–Torrey equation for a single value of the gradient.

The input of the algorithm consists in *physical* parameters (acquisition time t and diffusion coefficient D) and *numerical* parameters (number of trajectories N, surface layer thickness ε and reflection radius R). The choice of numerical parameters is a compromise between accuracy and rapidity.

- *Number of Brownian trajectories.* The number of trajectories N determines how accurately the expectation in Eq. (2) is approximated by Eq. (23). The statistical error of Monte Carlo simulations typically decreases as $1/\sqrt{N}$. Since the signal-to-noise ratio in diffusion-weighted NMR techniques is often between 100 and 1000, the choice of N between 10^4 and 10^6 allows for a reliable comparison to experimental results.
- *Surface layer thickness.* The surface layer thickness ε should be much smaller than the smallest geometrical feature of the boundary. In practice, this parameter can be chosen by computing the signal with several values of ε and finding such ε for which the resulting FID becomes independent of ε. Note that the computational time increases with ε *logarithmically slowly* that allows one to choose very small ε indeed.

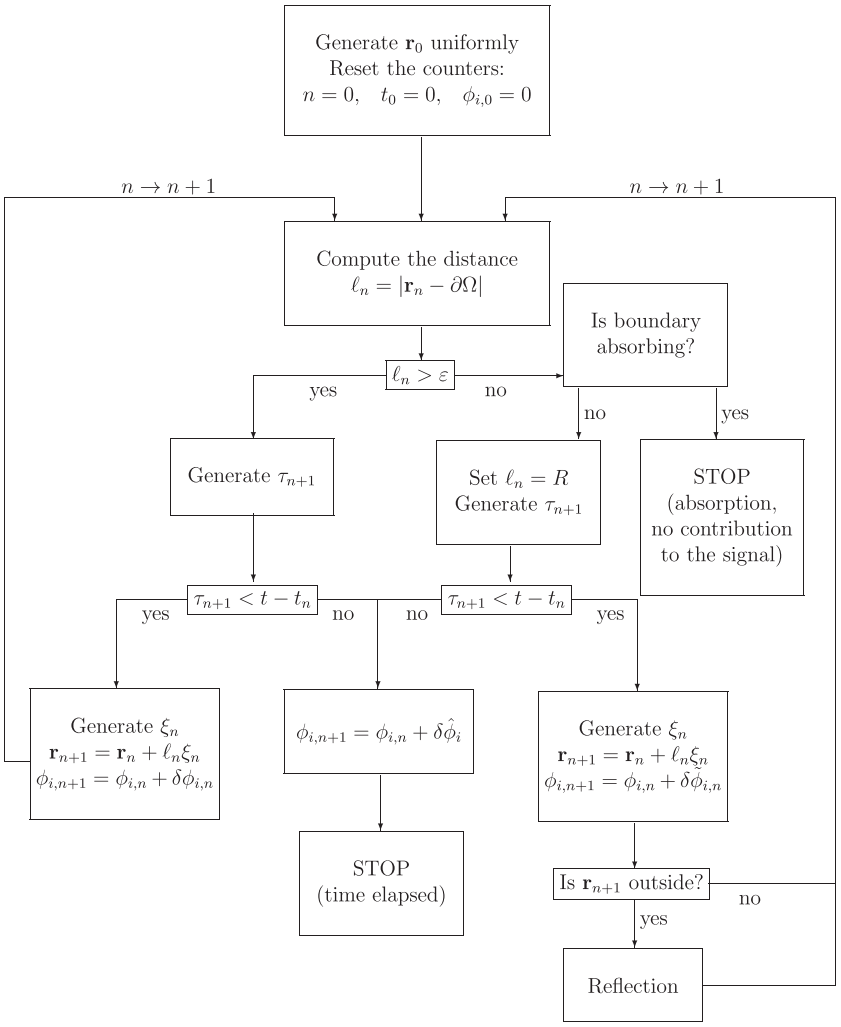

Fig. 4. Algorithmic scheme of one simulation run. The physical parameters (t,D) and numerical parameters (R,ε) are chosen prior to execution. The functions $S_0(t)$, $T_0(x)$, $\Phi_d(t)$, $\tilde{\Phi}_d(t)$ and $\hat{\Phi}_d(t)$ which had been computed and tabulated once and forever, are loaded prior to execution. The exit times τ_n are generated by Eq. (9). The random uniformly chosen positions ξ_n on the unit circle (sphere) are easy to generate. The phase increments $\delta\phi_{i,n}$, $\delta\hat{\phi}_i$ and $\delta\tilde{\phi}_{i,n}$ are given by Eqs. (12), (16) and (20), respectively. The shape of the diffusion-confining domain enters uniquely through three functions: (1) finding the distance $|\mathbf{r} - \partial\Omega|$ from any interior point $\mathbf{r}$ to the boundary $\partial\Omega$; (2) generating uniformly distributed initial position $\mathbf{r}_0$; and (3) computing the normal vector $\mathbf{n}$ at any boundary point. These functions have to be specifically designed for each confining domain.

- *Reflection radius.* After hitting the boundary, a particle is released at distance R from the hitting point. On the one hand, the reflection radius R has to be chosen as large as possible because the computational time is inversely proportional to R. On the other hand, this radius should be smaller than geometrical features of the boundary (otherwise, the computation of the mean phase shift for the half-disk or half-sphere would be inaccurate). There is no universal criterion for choosing R, the choice being dependent on the confining domain. A practical choice for R consists in computing the signal for different R and checking when the resulting FID becomes independent of R.

3. Discussion

The efficiency of a fast random walk algorithm significantly relies on fast computation of the distance to the boundary. In general, one can use hierarchical Whitney decomposition of the diffusion-confining domain or a set of "distance maps" at different length scales [36]. A specific geometrical structure of the domain (e.g., self-similarity) also helps to speed up the computation of the distance [37,38]. Since this problem is generic for fast random walk algorithms, while its solution is in turn specific for each confining domain, further discussion is beyond the scope of the paper. Similarly, the choice of the starting point (uniform or not) which should be realized specifically for each confining domain, is not discussed here.

3.1. Comparison between theory and simulations

We check the validity and accuracy of the developed fast random walk algorithm by calculating the FID by two different methods. On the one hand, the FID can be found using matrix formalisms [16,23,24]. This technique was shown to be very accurate for simple confining domains such as a sphere and a parallelepiped. Choosing these two domains for our consideration, we get "benchmark" signals for validating Monte Carlo results. On the other hand, we compute the empirical distributions of the normalized phases ϕ_i by our FRW algorithm. Fig. 5 shows the FID of water molecules ($D = 2 \times 10^{-9}$ m^2/s) diffusing inside the parallelepiped of size $L \times 2L \times 3L$ (with $L = 10^{-5}$ m) up to the acquisition time $t = 50$ ms. Each curve corresponds to the gradient oriented along one coordinate axis. Monte Carlo simulations were performed with $N = 10^5$ random walkers, $\varepsilon = 10^{-6}L$, and $R = 0.1L$. Even for such a large reflection radius, the agreement between these two approaches is excellent.

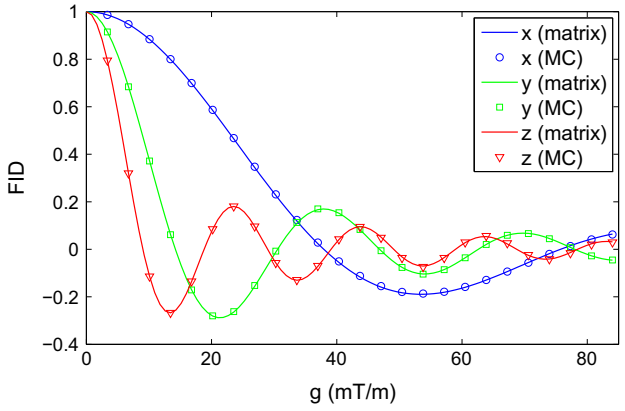

Fig. 5. The normalized FID as a function of the gradient intensity g inside the parallelepiped of size $L \times 2L \times 3L$, with $L = 10^{-5}$ m, $D = 2 \times 10^{-9}$ m^2/s and $t = 50$ ms. One can see an excellent agreement between the matrix formalism (considered as a "benchmark") and Monte Carlo simulations with $N = 10^5$ random walkers ($\varepsilon = 10^{-6}L, R = 0.1L$).

In order to access the accuracy of the algorithm in a more quantitative way, we compute the second moment of the empirical total dephasing

$$\mathbb{E}\{\phi_i^2\} \simeq \frac{1}{N}\sum_{j=1}^{N}(\phi_i^j)^2$$

and compare the normalized moment $\mathbb{E}\{\phi_i^2\}/t^2$ to its theoretical value given in Appendix D. In addition, we estimate the statistical error of the empirical second moment by computing $\mathbb{E}\{\phi_i^2\}/t^2$ from ten independent executions of the algorithm. The results for the unit sphere are shown in Table 1. The relative error of the empirical second moment (divided by t^2) as compared to the exact theoretical value is shown in percents. All relative errors are below 1%, and they all belong to the interval of statistical uncertainty. This is an accurate validation of the algorithm.

The last row of Table 1 shows CPU (in seconds) which required for this computation (realized on Dual Core AMD Opteron Processor 265 at 1.8 GHz, with RAM 4 GB). As expected, the CPU linearly increases with the acquisition time t as the number of jumps is approximately proportional to t. This linear increase is a typical drawback of most numerical techniques, including basic Monte Carlo simulations and basic finite difference or finite element methods (without adaptable time steps). The advantage of Monte Carlo techniques is a straightforward possibility of parallelization since the simulation runs are independent from each other. More importantly, *the computational time of fast random walk algorithms is known in general to be weakly dependent on the geometrical complexity* of the confining domain because the jump distance is always adapted to the local geometrical structure. A numerical study of these issues is currently in progress.

3.2. Time-dependent gradient

The FID signal corresponding to a time-independent gradient is the simplest PGSE measure for restricted diffusion. In practice, spin-echo or stimulated spin-echo sequences are often preferred [17]. In order to describe the related signal attenuation, an effective temporal profile $f(t)$ can be included into Eq. (1):

$$\varphi = \int_0^t dt' \gamma f(t') B(\mathbf{r}(t')).$$

For instance, the Hahn spin-echo sequence is described by $f(t') = 1$ for $0 < t' < t/2$ and $f(t') = -1$ for $t/2 < t' < t$. In theory, a given temporal profile $f(t')$ could be directly incorporated into Eq. (A.8) for the normalized mean phase $\mathbb{E}\{\phi\}$. The integral over time t_1 would

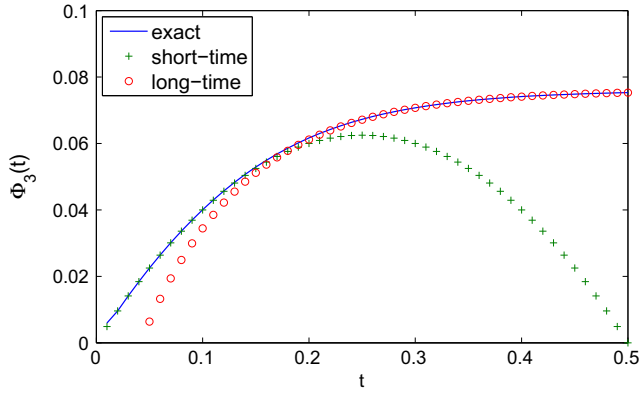

Fig. A.1. The function $\Phi_3(t)$ and the short-time and long-time asymptotic formulas (15) and (A.23) for the unit sphere. The two asymptotic curves cross at t around 0.18 (the "worst" point), for which the maximum relative error is around 1.7%. Similar results were obtained for the unit disk (not shown).

Table 1
Relative error of the second moment (divided by t^2) for the unit sphere (all the quantities here are dimensionless, with $L = 1$ and $D = 1$). The empirical phase distribution was computed by our Monte Carlo simulation with $N = 10^5$ particles, $\varepsilon = 10^{-6}$ and $R = 0.1$. Three rows show the relative error (in percents) of the empirical second moment as compared to the exact theoretical value. Numbers in parentheses indicate statistical errors (also in percents) of the empirical second moment. For all cases, the deviation from the theoretical value lies within the statistical uncertainty. The last row shows CPU (in seconds) which grows linearly with time t, as expected.

	$t = 0.01$	$t = 0.1$	$t = 1$	$t = 10$
x	0.53 (0.94)	0.77 (1.06)	0.69 (1.20)	0.39 (1.74)
y	0.02 (0.71)	0.22 (0.65)	0.55 (0.59)	0.31 (1.03)
z	0.04 (0.82)	0.51 (1.02)	0.43 (1.07)	0.29 (0.82)
CPU (s)	11	106	1059	10,508

then result in a modification of Eq. (A.8). In practice, however, this modification can lead to a drastic increase of the computational time. For simple spin-echo sequences with piecewise constant temporal profiles, it is therefore preferential to calculate the total dephasing successively for each time interval with a constant gradient. For instance, an implementation of the Hahn spin-echo encoding is as simple as that of the FID. In fact, one has $\varphi = \varphi_1 - \varphi_2$, with

$$\varphi_1 = \int_0^{t/2} dt' \gamma B(\mathbf{r}(t')), \quad \varphi_2 = \int_{t/2}^{t} dt' \gamma B(\mathbf{r}(t')),$$

where both φ_1 and φ_2 can be found by the FRW algorithm with few minor modifications.

3.3. Further extensions

Monte Carlo algorithms are acknowledged for their flexibility. In addition to the gradient encoding, various physical processes can be taken into account during the simulation of a random trajectory.

For instance, one can account for the enhanced attenuation due to bulk relaxation. In fact, since the duration of each jump is known, the corresponding attenuation factor (the probability of loosing magnetization during the jump) can be easily found. If the bulk relaxation rate is spatially uniform, all the nuclei are affected in the same way, and finding the common attenuation prefactor is trivial. If, on the opposite, there are regions with distinct bulk relaxation rates, the nucleus is affected differently in each region, and the cumulative attenuation factor can be found (however, the passage between two adjacent regions has to be considered in detail).

Surface relaxation is another common origin of signal attenuation. When the nucleus approaches the boundary close enough, it may experience the presence of magnetic impurities or strong local gradients due to susceptibility difference between the solid and void phases. The resulting attenuation can in general be computed in Monte Carlo simulations. However, the efficiency of the presented fast random walk algorithm relies significantly on reflection steps when a trajectory near the boundary is replaced by a single jump. In the presence of surface relaxation, the reflection step has to be revised in order to account for the possibility of loosing magnetization. This issue will be addressed in a future work.

In biological applications, the nuclei can diffuse inside one compartment and transfer to another one through a semi-permeable boundary. It seems possible to implement permeations in the fast random walk algorithm through the reflection step. When a particle reaches the semi-permeable boundary and has to make a reflection jump, one can randomly choose to which side of the boundary to place the particle, with a probability that depends on the permeability of the boundary (Fig. 3). Such an extension of the algorithm can be tested on multilayered structures for which an exact spectral solution was recently provided [39].

4. Conclusion

We proposed a new algorithm for computing pulsed-gradient spin-echo signal attenuation due to restricted diffusion in complex porous media. We showed that the gradient encoding can be incorporated into a fast random walk algorithm by summing the mean phase shifts during each jump. Since the simulation is continuously adapted to local length scales, the efficiency of the algorithm is weakly dependent on the geometrical complexity of the medium. The algorithm is a flexible numerical tool which can be implemented for computing the signal attenuation in hierarchical or multiscale porous media, ranging from model geometries (random packs of spheres and cylinders, fractals, percolation clusters, etc.) to complex natural structures (concrete, sandstones, sedimentary rocks, brain, lungs, etc.). The gradient encoding module (implemented in C) is provided on personal request.

Acknowledgment

The author thanks Dr. P. Tankov for fruitful discussions. The work has been partly supported by ANR grant "DYOPTRI".

Appendix A. Mean dephasing

In this Appendix, we compute the conditional expectation of the random variable

$$\phi = \int_0^t dt' B(\mathbf{w}_{t'}), \tag{A.1}$$

where $\mathbf{w}_{t'}$ is the Brownian motion which is started from a point $\mathbf{r}_{\rm ini}$ inside a confining domain Ω and conditioned to exit this domain at a fixed boundary point $\mathbf{r}_{\rm exit}$ at time t, without hitting the boundary $\partial\Omega$ until this time. As shown below, when Ω is the unit disk or sphere and $\mathbf{r}_{\rm ini}$ is its origin, the mean dephasing is

$$\mathbb{E}\{\phi\} = \Phi_d(t)\cos\theta, \tag{A.2}$$

where θ is the angle between the gradient $\mathbf{g}$ and the vector pointing from the origin towards the boundary point $\mathbf{r}_{\rm exit}$, and $\Phi_d(t)$ is given by Eqs. (13) and (14).

A.1. General confining domain

For a prescribed time t and prescribed initial and exit points $\mathbf{r}_{\rm ini}$ and $\mathbf{r}_{\rm exit}$, we introduce the joint probability for Brownian motion to exit a bounded domain Ω for the first time τ in an ε-vicinity of $\mathbf{r}_{\rm exit}$ and for τ to be in a δ-vicinity of t:

$$\begin{aligned} &P_t(\mathbf{r}_{\rm ini}, \mathbf{r}_{\rm exit}) = \mathbb{P}\{|\mathbf{w}_\tau - \mathbf{r}_{\rm exit}| < \varepsilon, \tau \in (t, t+\delta)\}, \\ &\tau = \min\{t' > 0 : \mathbf{w}_{t'} \in \partial\Omega\}. \end{aligned} \tag{A.3}$$

Since Brownian motion is a Markov process, the conditional expectation of ϕ for given $\mathbf{r}_{\rm ini}$, $\mathbf{r}_{\rm exit}$ and t can be written as

$$\mathbb{E}\{\phi\} = \frac{\int_0^t dt_1 \int_\Omega d\mathbf{r} G_{t_1}(\mathbf{r}_{\rm ini}, \mathbf{r}) B(\mathbf{r}) P_{t-t_1}(\mathbf{r}, \mathbf{r}_{\rm exit})}{P_t(\mathbf{r}_{\rm ini}, \mathbf{r}_{\rm exit})}, \tag{A.4}$$

where $G_t(\mathbf{r}_0, \mathbf{r})d\mathbf{r}$ is the probability to move from $\mathbf{r}_0$ to a $d\mathbf{r}$-vicinity of a point $\mathbf{r}$ in time t without hitting the boundary, and $G_t(\mathbf{r}_0, \mathbf{r})$ is the diffusion propagator or heat kernel with Dirichlet boundary condition on $\partial\Omega$:

$$\frac{\partial}{\partial t}G_t(\mathbf{r}_0,\mathbf{r}) - D\Delta G_t(\mathbf{r}_0,\mathbf{r}) = 0 \ (\mathbf{r}\in\Omega),$$
$$G_t(\mathbf{r}_0,\mathbf{r}) = 0 \ (\mathbf{r}\in\partial\Omega),$$
$$G_{t=0}(\mathbf{r}_0,\mathbf{r}) = \delta\ (\mathbf{r}-\mathbf{r}_0),$$

$\delta(\mathbf{r}-\mathbf{r}_0)$ being the Dirac distribution.

Eq. (A.4) has a clear probabilistic interpretation: a particle started from $\mathbf{r}_{\rm ini}$ first arrives at an intermediate time t_1 in a vicinity of a point $\mathbf{r}$ with probability $G_{t_1}(\mathbf{r}_{\rm ini},\mathbf{r})d\mathbf{r}$, without hitting the boundary. The dephasing is "probed" at this (random) point through the factor $B(\mathbf{r})$. After that, the particle diffuses inside Ω during the remaining time $t-t_1$ and exits the domain near point $\mathbf{r}_{\rm exit}$. The integrals stand for averaging over all intermediate points $\mathbf{r}$ and times t_1. The denominator expresses the conditional nature of the expectation (the fact that the exit point $\mathbf{r}_{\rm exit}$ and the exit time t are prescribed).

When ε and δ in Eq. (A.3) are small, the joint probability $P_t(\mathbf{r}_0,\mathbf{r})$ is described by its density $g_t(\mathbf{r}_0,\mathbf{r})$,

$$P_t(\mathbf{r}_0,\mathbf{r}) \approx \delta\varepsilon^{d-1}g_t(\mathbf{r}_0,\mathbf{r}),$$

where ε^{d-1} stands for the surface area of the ε-vicinity of the boundary point $\mathbf{r}$. Although the probability $P_t(\mathbf{r}_0,\mathbf{r})$ vanishes in the limit of ε and δ going to 0, the conditional expectation remains well-defined:

$$\mathbb{E}\{\phi\} = \frac{\int_0^t dt_1\int_\Omega d\mathbf{r}G_{t_1}(\mathbf{r}_{\rm ini},\mathbf{r})B(\mathbf{r})g_{t-t_1}(\mathbf{r},\mathbf{r}_{\rm exit})}{g_t(\mathbf{r}_{\rm ini},\mathbf{r}_{\rm exit})}. \tag{A.5}$$

We find that

$$g_t(\mathbf{r}_0,\mathbf{r}) = -D\frac{\partial G_t(\mathbf{r}_0,\mathbf{r})}{\partial n}, \tag{A.6}$$

where $\partial/\partial n$ is the normal derivative to the boundary directed toward the interior of the domain Ω.

The diffusion propagator has the spectral decomposition

$$G_t(\mathbf{r},\mathbf{r}') = \sum_m e^{-D\lambda_m t}u_m^*(\mathbf{r})u_m(\mathbf{r}'), \tag{A.7}$$

where the asterisk denotes the complex conjugate, and $u_m(\mathbf{r})$ and λ_m are the eigenfunctions and eigenvalues of the Laplace operator:

$$\Delta u_m(\mathbf{r}) + \lambda_m u_m(\mathbf{r}) = 0 \quad (\mathbf{r}\in\Omega),$$
$$u_m(\mathbf{r}) = 0 \quad (\mathbf{r}\in\partial\Omega).$$

The latter Dirichlet boundary condition guarantees that Brownian motion does not hit the boundary (since the contribution of the trajectories that have hit the boundary is equal to 0).

Using the spectral decomposition (A.7), the conditional expectation can be written as

$$\mathbb{E}\{\phi\} = \frac{\int_0^t dt_1\sum\limits_{m_1,m_2}U_{m_1}e^{-D\lambda_{m_1}t_1}\mathscr{B}_{m_1,m_2}e^{-D\lambda_{m_2}(t-t_1)}\widetilde{U}_{m_2}}{\sum\limits_m U_m\widetilde{U}_m e^{-D\lambda_m t}} \tag{A.8}$$

where

$$U_m = u_m^*(\mathbf{r}_{\rm ini}), \tag{A.9}$$

$$\widetilde{U}_m = -D\left(\frac{\partial u_m(\mathbf{r})}{\partial n}\right)_{\mathbf{r}=\mathbf{r}_{\rm exit}}, \tag{A.10}$$

$$\mathscr{B}_{m,m'} = \int_\Omega d\mathbf{r}\ u_m^*(\mathbf{r})\ B(\mathbf{r})\ u_{m'}(\mathbf{r}). \tag{A.11}$$

The integration over time yields

$$\mathbb{E}\{\phi\} = \frac{\sum\limits_m\left(I_m + U_m\mathscr{B}_{m,m}\widetilde{U}_m t\right)e^{-D\lambda_m t}}{\sum\limits_m U_m\widetilde{U}_m e^{-D\lambda_m t}}, \tag{A.12}$$

where

$$I_m = \sum_{m'\neq m}\frac{U_m\mathscr{B}_{m,m'}\widetilde{U}_{m'} + U_{m'}\mathscr{B}_{m',m}\widetilde{U}_m}{\lambda_{m'}-\lambda_m}. \tag{A.13}$$

These relations are applicable to any bounded domain Ω and arbitrary magnetic field $B(\mathbf{r})$. In the next two subsections, we give explicit formulas for these coefficients for a linear magnetic field gradient $B(\mathbf{r})$ inside the unit disk and sphere.

For the last step (see Section 2.3), a particle remains inside the disk until the exit time τ which exceeds the acquisition time t so that Eq. (A.5) becomes

$$\mathbb{E}\{\phi\} = \frac{\int_0^t dt_1\int_\Omega d\mathbf{r}G_{t_1}\ (\mathbf{r}_0,\mathbf{r})B\ (\mathbf{r})g_{\tau-t_1}(\mathbf{r},\mathbf{r}_{\rm exit})}{g_\tau(\mathbf{r}_0,\mathbf{r}_{\rm exit})}. \tag{A.14}$$

This first moment, for which a spectral decomposition similar to Eq. (A.8) can be easily written, depends on both time variables t and τ. Since this double dependence may be inconvenient for practical use, another solution for the last step will be presented in Appendix B.

A.2. The unit disk

For the unit disk with Dirichlet boundary condition, the Laplace operator eigenvalues and eigenfunctions are [41,42]

$$\lambda_{nk} = \alpha_{nk}^2, \quad u_{nk}(r,\theta) = \frac{\epsilon_n}{\sqrt{\pi}}\frac{1}{-J_n'(\alpha_{nk})}J_n(\alpha_{nk}r)\cos n\theta, \tag{A.15}$$

where $\epsilon_n = \sqrt{2}$ for $n>0$ and $\epsilon_0 = 1$, $J_n'(z)$ is the derivative of the Bessel function of the first kind, and $\{\alpha_{nk}\}_{k=0,\,1,\,2,\,\ldots}$ is the set of all positive zeros of the function $J_n(z)$ (with $n = 0,1,2,\ldots$). For convenience, the double index nk is used instead of the single index m to enumerate the eigenfunctions and eigenvalues. Similar notation is also adapted for the elements of the matrix $\mathscr{B}$ and vectors U and $\widetilde{U}$ (e.g., $\mathscr{B}_{nk,n'k'}$ is not a tensor of fourth rank but a matrix).

The elements of the matrix $\mathscr{B}$ for the linear magnetic field gradient $B(\mathbf{r}) = r\cos\theta$ have been calculated in [16,43]. In the case of Dirichlet boundary condition, we obtain

$$\mathscr{B}_{nk,n'k'} = \delta_{n,n'\pm1}(1+\delta_{n,0}+\delta_{n',0})^{1/2}\frac{2\alpha_{nk}\alpha_{n'k'}}{(\alpha_{nk}^2-\alpha_{n'k'}^2)^2}.$$

The elements of the vectors U and $\widetilde{U}$ are given by Eqs. (A.9) and (A.10). For the starting point $\mathbf{r}_{\rm ini} = (0,0)$ at the origin and the arrival point $\mathbf{r}_{\rm exit} = (\cos\theta,\sin\theta)$ on the boundary (the circle of radius 1), one gets

$$U_{nk} = \delta_{n,0}\frac{1}{\sqrt{\pi}J_1(\alpha_{0k})}, \tag{A.16}$$

$$\widetilde{U}_{nk} = D\frac{\epsilon_n}{\sqrt{\pi}}\alpha_{nk}\cos n\theta. \tag{A.17}$$

The above explicit formulas allow us to calculate the coefficients in Eq. (A.8):

$$U_{nk}\widetilde{U}_{nk} = \delta_{n,0}\frac{D\alpha_{0k}}{\pi J_1(\alpha_{0k})},$$
$$I_{nk} = \frac{4D\cos\theta}{\pi}\left[\delta_{n,0}\frac{\alpha_{0k}}{J_1(\alpha_{0k})}\sum_{k'=0}^{\infty}\frac{\alpha_{1k'}^2}{(\alpha_{1k'}^2-\alpha_{0k}^2)^3} + \delta_{n,1}\alpha_{1k}^2\sum_{k'=0}^{\infty}\frac{\alpha_{0k'}}{J_1(\alpha_{0k'})}\frac{1}{(\alpha_{0k'}^2-\alpha_{1k}^2)^3}\right].$$

The coefficients I_{nk} are proportional to $\cos\theta$, i.e., to the projection of the arrival point onto the gradient direction. Using the summation technique described in [44], one can compute the above sums over k' to get

$$U_{nk}\widetilde{U}_{nk} = \delta_{n,0}\frac{D\alpha_{0k}}{\pi J_1(\alpha_{0k})},$$
$$I_{nk} = \frac{D\cos\theta}{\pi}\left[\delta_{n,0}\frac{1}{2\alpha_{0k}J_1(\alpha_{0k})} + \delta_{n,1}\frac{1}{4J_0(\alpha_{1k})}\right]. \tag{A.18}$$

The presence of $\delta_{n,0}$ and $\delta_{n,1}$ reduces the summation over n in Eq. (A.8) yielding Eq. (13).

A.3. The unit sphere

The Laplace operator eigenvalues and eigenfunctions for the unit sphere with Dirichlet boundary condition are [41,42]

$$\lambda_{nk} = \alpha_{nk}^2, \quad u_{nk}(r,\theta) = \frac{\sqrt{2n+1}}{\sqrt{2\pi}} \frac{1}{-j_n'(\alpha_{nk})} j_n(\alpha_{nk} r) P_n(\cos\theta), \qquad (A.19)$$

where $j_n'(z)$ is the derivative of the spherical Bessel function of the first kind, $P_n(z)$ the Legendre polynomial, and $\{\alpha_{nk}\}_{k=0,\,1,\,2,\,\ldots}$ the set of all positive zeros of the function $j_n(z)$ (with $n = 0, 1, 2\ldots$). Since the applied magnetic field $B(\mathbf{r})$ is independent of the polar coordinate, we omitted this coordinate and the related third index for the eigenfunctions.

For the starting point $\mathbf{r}_{\rm ini}$ at the origin and the arrival point $\mathbf{r}_{\rm exit}$ on the boundary (the sphere of radius 1), one obtains

$$U_{nk} = \delta_{n,0} \frac{1}{\sqrt{2\pi} j_1(\alpha_{0k})}, \qquad (A.20)$$

$$\widetilde{U}_{nk} = D\sqrt{(2n+1)/(2\pi)}\,\alpha_{nk} P_n(\cos\theta). \qquad (A.21)$$

The explicit formula for the matrix $\mathscr{B}$ for a linear magnetic field gradient $B(\mathbf{r}) = r\cos\theta$ in the unit sphere was derived in [16,43]. In the case of Dirichlet boundary condition, one gets

$$\mathscr{B}_{nk,n'k'} = \delta_{n,n'\pm1} \frac{(n+n'+1)}{\sqrt{(2n+1)(2n'+1)}} \frac{2\alpha_{nk}\alpha_{n'k'}}{(\alpha_{nk}^2 - \alpha_{n'k'}^2)^2}.$$

Using the above relations, we obtain

$$U_{nk}\widetilde{U}_{nk} = \delta_{n,0} \frac{D\alpha_{0k}}{2\pi j_1(\alpha_{0k})},$$

$$I_{nk} = \frac{2D}{\pi}\cos\theta \left[\delta_{n,1}\alpha_{1k}^2 \sum_{k'=0}^{\infty} \frac{\alpha_{0k'}}{j_1(\alpha_{0k'})} \frac{1}{(\alpha_{1k}^2 - \alpha_{0k'}^2)^3} + \delta_{n,0} \frac{\alpha_{0k}}{j_1(\alpha_{0k})} \sum_{k'=0}^{\infty} \frac{\alpha_{1k'}^2}{(\alpha_{0k}^2 - \alpha_{1k'}^2)^3} \right].$$

Using the summation technique described in [44] and skipping technical details, we give the final result

$$\begin{aligned} U_{nk}\widetilde{U}_{nk} &= \delta_{n,0} D \frac{(-1)^k}{2\pi} \pi^2 (k+1)^2, \\ I_{nk} &= D \frac{(-1)^k}{8\pi} \cos\theta \left[3\delta_{n,0} - \sqrt{\alpha_{1k}^2 + 1}\,\delta_{n,1} \right]. \end{aligned} \qquad (A.22)$$

As for the unit disk, the coefficients I_{nk} are proportional to $\cos\theta$, that is to the projection of the arrival point onto the gradient direction. Once again, the presence of $\delta_{n,0}$ and $\delta_{n,1}$ reduces the summation over n yielding Eq. (14).

A.4. Asymptotic behavior of the normalized first moment

The conditional expectation of the dephasing ϕ is obtained in the spectral form (A.8) of infinite sums of exponential functions that nicely converge. For practical computation, smaller the time t, larger the number of terms that should be kept to get an accurate approximation. The major problem at small times is that both numerator and denominator of Eqs. (13) and (14) are very small so that their ratio $\Phi_d(t)$ is computed inaccurately. It is therefore helpful to derive an asymptotic formula for $\Phi_d(t)$ for small t. Using standard methods for investigating asymptotic behavior of the series involving the Laplace operator eigenvalues (e.g., see [16,44]), we obtain Eq. (15) for both cases $d = 2$ and $d = 3$. This relation is in fact very accurate for t smaller than 0.1 (for $t = 0.1$, the absolute error is of the order of 3.7×10^{-5} and the relative error is less than 0.2%).

The long-time behavior is simply obtained by keeping in Eqs. (13) and (14) the exponential terms with the smallest α_{nk}:

$$\Phi_d(t) \simeq \begin{cases} \frac{1}{2\alpha_{00}^2} + \frac{J_1(\alpha_{00})}{4\alpha_{00} J_0(\alpha_{10})} e^{-(\alpha_{10}^2 - \alpha_{00}^2)t} & (d=2), \\ \frac{3}{4\alpha_{00}^2} - \frac{\sqrt{\alpha_{10}^2+1}}{4\alpha_{00}^2} e^{-(\alpha_{10}^2 - \alpha_{00}^2)t} & (d=3). \end{cases} \qquad (A.23)$$

The accuracy of these asymptotic relations is illustrated on Fig. A.1.

Appendix B. Last jump

We propose the following approximate solution for simulating the last jump when the generated exit time τ_{n+1} exceeds the remaining time $t - t_n$ and the gradient encoding is switched off earlier. Since the position of the particle at time t is irrelevant, one can average the dephasing over all arrival points inside the unit disk (or ball). Since the rotational symmetry cancels the first moment, we focus on the second moment of the dephasing of a particle conditioned to survive up to time t. The survival probability is simply

$$S_0(t) = \int_\Omega d\mathbf{r} G_t(0,\mathbf{r}) = \sum_m U_m \widetilde{U}_m e^{-\lambda_m t}, \qquad (B.1)$$

where the starting point is at the origin, $U_m = u_m(0)$, and the arrival point is anywhere inside the domain:

$$\widetilde{U}_m = \int_\Omega d\mathbf{r} u_m(\mathbf{r}).$$

The conditional second moment is then the ratio between the second moment $S_2(t)$ for survived particles and the survival probability $S_0(t)$: $\mathbb{E}\{\phi^2\} = S_2(t)/S_0(t)$, where [16]

$$S_2(t) = 2\int_0^t dt_1 \int_{t_1}^t dt_2 \int_\Omega d\mathbf{r}_1 \int_\Omega d\mathbf{r}_2 \int_\Omega d\mathbf{r}_3 G_{t_1}(0,\mathbf{r}_1) B(\mathbf{r}_1) G_{t_2-t_1}(\mathbf{r}_1,\mathbf{r}_2)$$

$$B(\mathbf{r}_2) G_{t-t_2}(\mathbf{r}_2,\mathbf{r}_3) = 2 \sum_{m_1,m_2,m_3} U_{m_1} \mathscr{B}_{m_1,m_2} \mathscr{B}_{m_2,m_3} \widetilde{U}_{m_3} F(t,\lambda_{m_1},\lambda_{m_2},\lambda_{m_3})$$

and

$$F(t,\lambda_{m_1},\lambda_{m_2},\lambda_{m_3}) = \int_0^t dt_1 \int_{t_1}^t dt_2 e^{-\lambda_{m_1} t_1} e^{-\lambda_{m_2}(t_2-t_1)} e^{-\lambda_{m_3}(t-t_2)}.$$

In both two and three dimensions, the double index nk is used instead of m. The Kronecker symbols $\delta_{n,0}$ in U_{nk} and $\widetilde{U}_{nk}$, and $\delta_{n,n'\pm1}$ in $\mathscr{B}_{nk,n'k'}$ reduce the summation to

$$S_2(t) = 2 \sum_{k_1,k_2,k_3} U_{0,k_1} \mathscr{B}_{0k_1,1k_2} \mathscr{B}_{1k_2,0k_3} \widetilde{U}_{0k_3} F(t,\lambda_{0k_1},\lambda_{1k_2},\lambda_{0k_3}),$$

where the function F for $k_1 \neq k_3$ reads as

$$F(t,\lambda_{0k_1},\lambda_{1k_2},\lambda_{0k_3}) = \frac{1}{\lambda_{0k_3} - \lambda_{1k_2}} \left[\frac{e^{-\lambda_{0k_1}t} - e^{-\lambda_{1k_2}t}}{\lambda_{1k_2} - \lambda_{0k_1}} - \frac{e^{-\lambda_{0k_1}t} - e^{-\lambda_{0k_3}t}}{\lambda_{0k_3} - \lambda_{0k_1}} \right],$$

and for $k_1 = k_3$

$$F(t,\lambda_{0k_1},\lambda_{1k_2},\lambda_{0k_3}) = \frac{1}{\lambda_{0k_3} - \lambda_{1k_2}} \left[\frac{e^{-\lambda_{0k_1}t} - e^{-\lambda_{1k_2}t}}{\lambda_{1k_2} - \lambda_{0k_1}} - te^{-\lambda_{0k_3}t} \right].$$

In what follows, we provide the explicit formula for $S_2(t)$ for the unit disk and the unit sphere.

B.1. The unit disk

For the unit disk, Eq. (A.15) yields

$$\widetilde{U}_{nk} = \delta_{n,0} \frac{2\sqrt{\pi}}{\alpha_{0k}},$$

Combining with Eq. (A.16) for U_{nk}, one gets Eq. (4) for the survival probability $S_0(t)$, and

$$S_2(t) = 32 \sum_{k_1,k_2,k_3} \frac{\alpha_{0k_1}}{J_1(\alpha_{0k_1})} \frac{\alpha_{1k_2}^2}{(\alpha_{0k_1}^2 - \alpha_{1k_2}^2)^2} \times \frac{1}{(\alpha_{1k_2}^2 - \alpha_{0k_3}^2)^2} F(t, \lambda_{0k_1}, \lambda_{1k_2}, \lambda_{0k_3}).$$

Although this triple sum can already be computed numerically, the Laplace transform summation technique [16,44] allows us to further simplify the formula. In fact, two of the three sums can be calculated analytically that yields Eq. (18). This is an exact explicit formula which is particularly convenient for numerical computations.

In order to investigate the short-time behavior of the function $S_2(t)$, we derive another exact representation for $S_2(t)$ by using Laplace transforms:

$$S_2(t) = \frac{2}{3}t^3 - \frac{1}{96}\mathscr{L}^{-1}\left[\frac{3s^2+56s+288}{s^4 I_0(\sqrt{s})}\right](t) + \frac{1}{4}\mathscr{L}^{-1}\left[\frac{1}{s^{5/2} I_1(\sqrt{s})}\right](t) + \frac{t}{12}\mathscr{L}^{-1}\left[\frac{s-4}{s^3 I_0(\sqrt{s})}\right](t), \quad \text{(B.2)}$$

where $I_n(z)$ is the modified Bessel function of the first kind, and $\mathscr{L}^{-1}$ denotes the inverse Laplace transform. In the limit $t \to 0$, one derives

$$S_2(t) = \frac{2}{3}t^3 - \frac{e^{-1/(4t)}t^2}{4}(1 + O(t)).$$

Since the function $e^{-1/(4t)}$ decreases extremely fast as $t \to 0$, the first term $2t^3/3$ representing the second moment for unrestricted diffusion, is a very accurate approximation of $S_2(t)$ in this limit.

Note that the survival probability $S_0(t)$ can also be represented through the inverse Laplace transform as

$$S_0(t) = 1 - \mathscr{L}^{-1}\left[\frac{1}{\sqrt{s} I_0(\sqrt{s})}\right](t).$$

B.2. The unit sphere

For the unit sphere, Eq. (A.19) yields

$$\widetilde{U}_{nk} = \delta_{n,0}\frac{2\sqrt{2\pi}}{\alpha_{0k}}.$$

Combining with Eq. (A.20) for U_{nk}, one gets Eq. (5) for the survival probability $S_0(t)$, and

$$S_2(t) = \frac{64}{3} \sum_{k_1,k_2,k_3} (-1)^{k_1} \frac{\lambda_{0k_1}\lambda_{1k_2}}{(\lambda_{0k_1} - \lambda_{1k_2})^2} \times \frac{1}{(\lambda_{1k_2} - \lambda_{0k_3})^2} F(t, \lambda_{0k_1}, \lambda_{1k_2}, \lambda_{0k_3}).$$

As earlier, the Laplace transform summation technique [16,44] allows us to compute two of the three sums analytically that yields the exact formula (19). Another exact representation for $S_2(t)$ can be derived by Laplace transforms:

$$S_2(t) = \frac{2t^3}{3} - \frac{1}{24}\mathscr{L}^{-1}\left[\frac{s^2+17s+174}{2s^{7/2}\sinh\sqrt{s}}\right](t) + \frac{5}{24}\mathscr{L}^{-1}\left[\frac{1}{s^{3/2}(\sinh\sqrt{s} - \sqrt{s}\cosh\sqrt{s})}\right](t) + \frac{t}{24}\mathscr{L}^{-1}\left[\frac{4s-3}{s^{5/2}\sinh\sqrt{s}}\right](t).$$

In the limit $t \to 0$, one finds

$$S_2(t) = \frac{2}{3}t^3 - \frac{e^{-1/(4t)}t^{3/2}}{\sqrt{\pi}}(1 + O(t)).$$

As previously, the second term decays extremely fast as $t \to 0$ so that $2t^3/3$ is a very accurate approximation of $S_2(t)$ in this limit.

Note that the survival probability $S_0(t)$ can also be represented through the inverse Laplace transform

$$S_0(t) = 1 - \mathscr{L}^{-1}\left[\frac{1}{\sqrt{s}\sinh\sqrt{s}}\right](t).$$

Its inversion can be performed explicitly yielding another exact representation

$$S_0(t) = 1 - \frac{2}{\sqrt{\pi}\sqrt{t}}\sum_{k=1}^{\infty} e^{-(2k-1)^2/(4t)}.$$

This formula is complementary to Eq. (5).

Appendix C. Reflection step

The length of reflection jumps is a limiting factor of the algorithm. Once the reflected Brownian motion reached the boundary, it would repeatedly return to the boundary for a while. The algorithm would therefore produce many tiny jumps that would significantly slow down the simulation. It is therefore important to "release" a particle as far as possible from the boundary. If the boundary is (almost) flat, one could draw a half-circle (half-sphere) around the current boundary point and make a large jump to a uniformly chosen point on this half-circle. The "only" question is how to compute the phase accumulated during this jump.

Although the spectral approach is applicable in this case, there is no explicit formula for the elements of the matrix $\mathscr{B}$ for a half-disk (or half-sphere). More importantly, if one tried to proceed the computation of Appendix A, the mean dephasing $\mathbb{E}\{\phi\}$ would not be proportional to $\cos\theta$ (as it was for a linear gradient in a sphere or a disk), but it would be represented as a series containing infinitely many terms $\cos n\theta$ with complicated time-dependent coefficients. Such a numerical computation, though still feasible, would be too time-consuming.

In order to overcome this problem, we propose to average the mean dephasing over all arrival points on the half-circle (half-sphere). This means that, whatever the randomly chosen arrival point is, the average dephasing during the jump is added. In contrast to the whole disk, for which the average dephasing was zero (due to the symmetry), the contribution for the half-disk is nontrivial. Since the number of reflections from the boundary is typically much smaller than the number of "ordinary" jumps, this approximation should not degrade the accuracy.

C.1. Perpendicular gradient direction

First, we consider the case when the applied gradient is perpendicular to the base of the half-disk. The dephasing in the upper half-disk with a linear gradient $B(\mathbf{r}) = y$ is equivalent to the dephasing in the whole disk with the magnetic field $\widetilde{B}(\mathbf{r}) = |y|$. The above formalism can be applied if the usual matrix $\mathscr{B}$ is replaced by

$$\widetilde{\mathscr{B}}_{m,m'} = \int_\Omega d\mathbf{r}\; u_m^*(\mathbf{r})|y|\; u_{m'}(\mathbf{r}).$$

The averaging over all arrival points modifies the vector $\widetilde{U}$:

$$\widetilde{U}_{nk} = -\frac{D}{S}\int_{\partial\Omega} d\mathbf{r}\frac{\partial u_{nk}(\mathbf{r})}{\partial n},$$

where S is the surface area of the domain. We find

$$\widetilde{U}_{nk} = \delta_{n,0}\frac{D\alpha_{0k}}{\sqrt{\pi}} \quad (d=2),$$

$$\widetilde{U}_{nk} = \delta_{n,0}\frac{D\alpha_{0k}}{\sqrt{2\pi}} \quad (d=3).$$

The whole point of averaging over the arrival points was to get the Kronecker symbol $\delta_{n,0}$ which reduces the summation over n in Eq.

(A.13) for I_{nk} and eliminates the dependence on $\cos n\theta$. Note that the vector U representing the starting from the origin remains unchanged.

In the three-dimensional case, we obtain

$$I_{nk} = \frac{\delta_{n,0}}{2\pi} \sum_{k' \neq k} \frac{\widetilde{\mathscr{B}}_{0k,0k'}}{\lambda_{0k'} - \lambda_{0k}} \left(\frac{\alpha_{0k'}}{j_1(\alpha_{0k})} + \frac{\alpha_{0k}}{j_1(\alpha_{0k'})} \right).$$

where

$$\widetilde{\mathscr{B}}_{0k,0k'} = \int_0^1 dr r^3 \frac{j_0(\alpha_{0k} r)}{j_0'(\alpha_{0k})} \frac{j_0(\alpha_{0k'} r)}{j_0'(\alpha_{0k'})}.$$

Using $\alpha_{0k} = \pi(k+1)$, $j_0(x) = \sin(x)/x$ and $j_1(x) = \sin(x)/x^2 - \cos(x)/x$, one has

$$\widetilde{\mathscr{B}}_{0k,0k'} = \frac{2}{(\lambda_{0k} - \lambda_{0k'})^2} \left[\alpha_{0k}\alpha_{0k'} - \frac{1}{j_1(\alpha_{0k}) j_1(\alpha_{0k'})} \right]$$

for $k \neq k'$, and $\widetilde{\mathscr{B}}_{0k,0k} = 1/4$. A direct computation yields $I_{nk} = 0$, so that

$$\widetilde{\Phi}_3(t) \equiv \mathbb{E}\{\tilde{\phi}\} = t \frac{\sum_{k=0}^{\infty} U_{0k} \widetilde{\mathscr{B}}_{0k,0k} \widetilde{U}_{0k} e^{-\lambda_{0k} t}}{\sum_{k=0}^{\infty} U_{0k} \widetilde{U}_{0k} e^{-\lambda_{0k} t}} = \frac{t}{4}.$$

This astonishingly simple result for the half-sphere relies on the fact that $\widetilde{\mathscr{B}}_{0k,0k} = 1/4$ is independent of k and factored out from the sum in the numerator.

This is not true for the half-disk for which

$$I_{nk} = \frac{\delta_{n,0}}{\pi} \sum_{k' \neq k} \frac{\widetilde{\mathscr{B}}_{0k,0k'}}{\lambda_{0k'} - \lambda_{0k}} \left(\frac{\alpha_{0k'}}{J_1(\alpha_{0k})} + \frac{\alpha_{0k}}{J_1(\alpha_{0k'})} \right),$$

where

$$\widetilde{\mathscr{B}}_{0k,0k'} = \int_0^1 dr r^2 \frac{J_0(\alpha_{0k} r)}{J_0'(\alpha_{0k})} \frac{J_0(\alpha_{0k'} r)}{J_0'(\alpha_{0k'})}.$$

The integral has to be computed numerically. We find that $\widetilde{\mathscr{B}}_{0k,0k}$ is not a constant any more, but it approaches a constant as k increases. The computation of the mean dephasing $\mathbb{E}\{\tilde{\phi}\}$ is therefore more complicated, although it can still be performed numerically according to

$$\widetilde{\Phi}_2(t) = \frac{\sum_{k=0}^{\infty} \left(\pi I_{0k} + t \frac{\alpha_{0k}}{J_1(\alpha_{0k})} \widetilde{\mathscr{B}}_{0k,0k} \right) e^{-\alpha_{0k}^2 t}}{\sum_{k=0}^{\infty} \frac{\alpha_{0k}}{J_1(\alpha_{0k})} e^{-\alpha_{0k}^2 t}}.$$

Denoting

$$i_k^{(1)} = \pi I_{0k},$$
$$i_k^{(2)} = \frac{\alpha_{0k}}{J_1(\alpha_{0k})} \left(\frac{1}{4} - \widetilde{\mathscr{B}}_{0k,0k} \right), \tag{C.1}$$

one gets Eq. (21). The coefficients I_{0k} and $\widetilde{\mathscr{B}}_{0k,0k}$, as well as the function $\widetilde{\Phi}_2(t)$ itself, have to be computed only once, while their tabulated values can be loaded before starting Monte Carlo simulations.

C.2. Arbitrary orientation

In general, the orientation of the half-disk (or half-sphere) is not parallel to the applied gradient. In this case, the dephasing along any gradient direction is decomposed into two contributions: the dephasing $\phi_{\parallel} = \Phi_d(t)$ in the plane which is parallel to the base of the half-disk (Appendix A), and the dephasing $\phi_{\perp} = \widetilde{\Phi}_d(t)$ which was just computed. It is crucial that Brownian motions in parallel and perpendicular directions are independent, although they will be stopped at the same time when the particle exits from the sphere.

Let $\mathbf{n}$ be the normal vector determining the orientation of the half-disk, and $\mathbf{r}$ is the unit vector pointing towards the arrival (exit) point (Fig. 3). The normalized projection of $\mathbf{r}$ onto the base of the half-disk is

$$\mathbf{n}_{\mathbf{r}} = \frac{\mathbf{r} - \mathbf{n}(\mathbf{r}\cdot\mathbf{n})}{|\mathbf{r} - \mathbf{n}(\mathbf{r}\cdot\mathbf{n})|}.$$

Projections of the "dephasing vector" $\mathbf{f} = \phi_{\perp}\mathbf{n} + \phi_{\parallel}\mathbf{n}_{\mathbf{r}}$ onto the coordinate axes, $(\mathbf{f}\cdot\mathbf{e}_i)$, yield the contributions to each phase counter according to Eq. (20).

Appendix D. Second moment of the total dephasing

We briefly recall the computation of the second moment of the total dephasing for the FID. Following [16], one can write

$$\mathbb{E}\{\phi^2/2\} = \sum_m \mathscr{B}_{0,m}^2 \int_0^1 dt_1 \int_{t_1}^1 dt_2 e^{-p(t_2 - t_1)\lambda_m} = \frac{1}{p}\zeta_{-1} - \frac{1}{p^2}\zeta_{-2} + \frac{1}{p^2} \sum_m \mathscr{B}_{0,m}^2 \lambda_m^{-2} e^{-p\lambda_m}, \tag{D.1}$$

where $p = Dt/L^2$ is the dimensionless diffusion coefficient, and

$$\zeta_{-k} = \sum_m \mathscr{B}_{0,m}^2 \lambda_m^{-k} \quad (k = 1, 2, 3, \ldots).$$

For slab, cylinder and sphere with reflecting boundary (Neumann boundary condition), the matrix elements $\mathscr{B}_{0,m}$ and the eigenvalues λ_m are given in [16]. In particular, one finds

$$\mathbb{E}\{\phi^2/2\} = \tfrac{1}{120}p^{-1} - \tfrac{17}{20160}p^{-2} + p^{-2}\tfrac{8}{\pi^4}\sum_{k=0}^{\infty}\tfrac{e^{-p\pi^2(2k+1)^2}}{(2k+1)^4} \quad (d=1),$$
$$\mathbb{E}\{\phi^2/2\} = \tfrac{7}{96}p^{-1} - \tfrac{11}{512}p^{-2} + 2p^{-2}\sum_{k=0}^{\infty}\tfrac{e^{-p\lambda_{1k}}}{\lambda_{1k}^3(\lambda_{1k}-1)} \quad (d=2),$$
$$\mathbb{E}\{\phi^2/2\} = \tfrac{8}{175}p^{-1} - \tfrac{83}{7875}p^{-2} + 2p^{-2}\sum_{k=0}^{\infty}\tfrac{e^{-p\lambda_{1k}}}{\lambda_{1k}^3(\lambda_{1k}-2)} \quad (d=3). \tag{D.2}$$

These exact formulas were used for computing the second moment shown in Table 1.

References

[1] K.R. Brownstein, C.E. Tarr, Importance of classical diffusion in NMR studies of water in biological cells, Phys. Rev. A 19 (1979) 2446–2453.
[2] L.L. Latour, K. Svoboda, P.P. Mitra, C.H. Sotak, Time-dependent diffusion of water in a biological model system, Proc. Natl. Acad. Sci. USA 91 (1994) 1229–1233.
[3] C. Nicholson, Diffusion and related transport mechanisms in brain tissue, Rep. Prog. Phys. 64 (2001) 815–884.
[4] Y. Assaf, R.Z. Freidlin, G.K. Rohde, P.J. Basser, New modeling and experimental framework to characterize hindered and restricted water diffusion in brain white matter, Magn. Reson. Med. 52 (2004) 965–978.
[5] D. Le Bihan, C. Poupon, A. Amadon, F. Lethimonnier, Artifacts and pitfalls in diffusion MRI, J. Magn. Reson. Imag. 24 (2006) 478–488.
[6] V.G. Kiselev, K.A. Il'yasov, Is the 'biexponential diffusion' biexponential?, Magn Reson. Med. 57 (2007) 464.
[7] G.F. Froment, K.B. Bischoff, Chemical Reactor Analysis and Design, Wiley, New York, 1980.
[8] C.H. Bartholomew, Mechanisms of catalyst deactivation, Appl. Catal. A: Gen. 212 (2001) 17–60.
[9] M. Filoche, D.S. Grebenkov, J.S. Andrade Jr., B. Sapoval, Passivation of irregular surfaces accessed by diffusion, Proc. Natl. Acad. Sci. 105 (2008) 7636–7640.
[10] R.W. Mair, G.P. Wong, D. Hoffmann, M.D. Hürlimann, S. Patz, L.M. Schwartz, R.L. Walsworth, Probing porous media with gas diffusion NMR, Phys. Rev. Lett. 83 (1999) 3324.
[11] Y.-Q. Song, S. Ryu, P.N. Sen, Determining multiple length scales in rocks, Nature 406 (2000) 178.
[12] R.C. Wilson, M.D. Hürlimann, Relationship between susceptibility induced field inhomogeneities, restricted diffusion, and relaxation in sedimentary rocks, J. Magn. Reson. 183 (2006) 1.
[13] N. Nestle, P. Galvosas, O. Geier, M. Dakkouri, C. Zimmermann, J. Kärger, NMR studies of water diffusion and relaxation in hydrating slag-based construction materials, Magn. Reson. Imag. 19 (2001) 547–548.
[14] P.J. McDonald, J.-P. Korb, J. Mitchell, L. Monteilhet, Surface relaxation and chemical exchange in hydrating cement pastes: a two-dimensional NMR relaxation study, Phys. Rev. E 72 (2005) 011409-1–011409-9.

[15] P.N. Sen, Time-dependent diffusion coefficient as a probe of geometry, Concepts Magn. Reson. 23A (2004) 1–21.
[16] D.S. Grebenkov, NMR survey of reflected Brownian motion, Rev. Mod. Phys. 79 (2007) 1077–1137.
[17] P.T. Callaghan, Principles of Nuclear Magnetic Resonance Microscopy, Clarendon, Oxford, 1991.
[18] A.T. Watson, C.T.P. Chang, Characterizing porous media with NMR methods, Prog. Nucl. Magn. Reson. Spectrosc. 31 (1997) 343–386.
[19] Y.-Q. Song, Using internal magnetic fields to obtain pore size distribution of porous media, Conc. Magn. Reson. 18A (2003) 97–110.
[20] M.S. Conradi, B. Saam, D.A. Yablonskiy, J.C. Woods, Hyperpolarized 3He and perfluorocarbon gas diffusion MRI of lungs, Prog. Nucl. Magn. Reson. Spectrosc. 48 (2006) 63–83.
[21] D. Le Bihan, Looking into the functional architecture of the brain with diffusion MRI, Nat. Rev. Neurosci. 4 (2003) 469–480.
[22] E. Özarslan, Compartment shape anisotropy (CSA) revealed by double pulsed field gradient MR, J. Magn. Reson. 199 (2009) 56.
[23] D.S. Grebenkov, Laplacian eigenfunctions in NMR I. A numerical tool, Conc. Magn. Reson. 32A (2008) 277–301.
[24] D.S. Grebenkov, Laplacian eigenfunctions in NMR II. Theoretical advances, Conc. Magn. Reson. 34A (2009) 264–296.
[25] B.D. Hughes, Random Walks and Random Environments, Clarendon Press, Oxford, 1995.
[26] K.K. Sabelfeld, Monte Carlo Methods in Boundary Value Problems, Springer-Verlag, New York, Heidelberg, Berlin, 1991.
[27] B. Balinov, B. Jönsson, P. Linse, O. Söderman, The NMR self-diffusion method applied to restricted diffusion. simulation of echo attenuation from molecules in spheres and between planes, J. Magn. Reson. A 104 (1993) 17–25.
[28] P. Linse, O. Söderman, The validity of the short-gradient-pulse approximation in NMR studies of restricted diffusion. Simulations of molecules diffusing between planes, in cylinders and spheres, J. Magn. Reson. A 116 (1995) 77–86.
[29] A. Duh, A. Mohorič, J. Stepišnik, Computer simulation of the spin-echo signal distribution in the case of restricted self-diffusion, J. Magn. Reson. 148 (2001) 257–266.
[30] R.M.E. Valckenborg, H.P. Huinink, J.J.v.d. Sande, K. Kopinga, Random-walk simulations of NMR dephasing effects due to uniform magnetic-field gradients in a pore, Phys. Rev. E 65 (2002) 021306-1–021306-8.
[31] D.S. Grebenkov, G. Guillot, B. Sapoval, Restricted diffusion in a model acinar labyrinth by NMR. Theoretical and numerical results, J. Magn. Reson. 184 (2007) 143–156.
[32] M. Leibig, Random walks and NMR measurements in porous media, J. Phys. A: Math. Gen. 26 (1993) 3349–3367.
[33] M.E. Muller, Some continuous Monte Carlo methods for the Dirichlet problem, Ann. Math. Stat. 27 (1956) 569–589.
[34] L.H. Zheng, Y.C. Chiew, Computer simulation of diffusion-controlled reactions in dispersions of spherical sinks, J. Chem. Phys. 90 (1989) 322–327.
[35] S.B. Lee, I.C. Kim, C.A. Miller, S. Torquato, Random-walk simulation of diffusion-controlled processes among static traps, Phys. Rev. B 39 (1989) 11833–11839.
[36] P. Ossadnik, Multiscaling analysis of large-scale off-lattice DLA, Physica A 176 (1991) 454.
[37] D.S. Grebenkov, What makes a boundary less accessible, Phys. Rev. Lett. 95 (2005) 200602.
[38] D.S. Grebenkov, A.A. Lebedev, M. Filoche, B. Sapoval, Multifractal properties of the harmonic measure on Koch boundaries in two and three dimensions, Phys. Rev. E 71 (2005) 056121.
[39] D.S. Grebenkov, Pulsed-gradient spin-echo monitoring of restricted diffusion in multilayered structures, J. Magn. Reson. 205 (2010) 181–195.
[41] J. Crank, The Mathematics of Diffusion, second ed., Clarendon, Oxford, 1975.
[42] H.S. Carslaw, J.C. Jaeger, Conduction of Heat in Solids, second ed., Clarendon, Oxford, 1959.
[43] D.S. Grebenkov, Analytical solution for restricted diffusion in circular and spherical layers in inhomogeneous magnetic fields, J. Chem. Phys. 128 (2008) 134702.
[44] D.S. Grebenkov, Multiple correlation function approach: rigorous results for simple geometries, Diff. Fundam. 5 (2007) 1–34.